ChemPubSoc Europe

DOI: 10.1002/cctc.201601042

CHEMCATCHEM Full Papers

Butanal Condensation Chemistry Catalyzed by Brønsted Acid Sites on Polyoxometalate Clusters

Yifei Yang, Fan Lin, Honghi Tran, and Ya-Huei (Cathy) Chin*[a]

The connection of active site structures and their catalytic chemistry during butanal deoxygenation on polyoxometalate clusters with varying H^+ site densities and identity of central atoms [$H_xNa_{4-x}SiW_{12}O_{40}$ ($x=0$–4) and $H_yNa_{3-y}PW_{12}O_{40}$ ($y=0$–3)] was established with rate assessment, IR spectroscopic, and chemical titration methods. Butanal adsorbs on the H^+ or Na^+ ions on polyoxometalate clusters and forms RC=O···H^+ or RC=O···Na^+ complexes at 348 K. A portion of the adsorbed butanals on the H^+ sites converts to surface acetates through their reactions with vicinal framework oxygen atoms, as confirmed from the detection of ν_{as}(OCO) band at approximately 1580 cm^{-1}, and remains as the spectator species. Bimolecular reactions of butanals on the remaining H^+ sites lead to 2-ethyl-2-hexenal as the predominant products, within which a small fraction undergoes sequential cyclization–dehydration to produce aromatics. A trace amount of butanal converts through minor, competitive pathways that form light olefins and dienes. These findings on the connection between active sites and their catalytic chemistry provide mechanistic insights useful for tuning the rates of the various concomitant paths and thus yields towards the different products during deoxygenation reactions.

Introduction

Catalytic deoxygenation removes oxygen atoms from biomass-derived oxygenates, thus increasing their heating values and thermal stabilities as a step towards the sustainable synthesis of fuels and value-added chemicals.[1] Solid Brønsted acids such as H-ZSM-5 and H-FAU zeolites are attractive catalysts for the deoxygenation of light alkanals (R–CHO; e.g., R = C_2H_5)[1b,2] or alkanones ($R^1C{=}OR^2$; e.g., $R^1=C_2H_5$, $R^2=CH_3$)[3] at atmospheric pressure and without the consumption of external H_2. Specifically, acid-catalyzed deoxygenation of propanal on H-ZSM-5 leads to alkenes, larger unsaturated aldehydes, and diverse aromatics (e.g., mono-, di-, and trimethylbenzenes).[2] Among these products, unsaturated aldehydes are important intermediates for the production of fine chemicals used for perfumes,[4] flavors,[5] and pharmaceutical products.[6] For example, acrolein and 2-ethyl-2-hexenal are attractive intermediates produced via aldol type C–C bond coupling reactions between acetaldehyde and formaldehyde[7] and between two butanal molecules,[8] respectively. These reactions require the initial activation of aldehydes at Brønsted acid sites (H^+).

Small aldehydes or ketones adsorb at Brønsted acid sites via their carbonyl oxygen atoms, forming hydrogen-bonded complexes (RC=O···H^+), as concluded from IR and NMR studies and quantum-chemical calculations (e.g., acetaldehyde on H-ZSM-5[9] and acetone on H-ZSM-5).[10] The adsorption causes protonation of the carbonyl groups and polarization of the adsorbates.[10c] The proton transfer weakens the C=O bond and shifts its vibrational frequencies to lower wavenumbers, as found previously for acetaldehyde adsorption on H-ZSM-5, during which the C=O vibrational frequencies shift from 1725 cm^{-1} to 1686 cm^{-1}.[9] Separate density functional theory (DFT) calculations confirmed such perturbations from a bond elongation between the lattice oxygen atom of ZSM-5 and H^+ from 0.97 to 1.04 Å.[11] The hydrogen-bonded complexes (RC=O···H^+) are in chemical equilibrium with their protonated forms (RC^+–O–H),[12] because of small differences in their heats of adsorption. For example, the energy difference between chemisorbed and physisorbed acetaldehyde on H-ZSM-5 is approximately 6 kJ mol^{-1}.[13] Replacing the Brønsted acid sites with alkali cations leads to aldehyde or ketone adsorption on these cations as cationic bonded complexes (RC=O···M^{n+}), as evidenced from the detection of C=O vibrational bands at approximately 1715 cm^{-1} with IR spectroscopy during acetaldehyde adsorption on Li^+, Na^+, K^+, Ca^{2+}, Ni^{2+}, or Al^{3+} cation-exchanged montmorillonites.[14] Such interactions reflect the polarization of carbonyl groups by the cationic sites and weakening of the C=O bond;[10c] these effects may in turn affect their reactivities in deoxygenation reactions.

The mechanism for aldol condensation reactions on solid Brønsted acid and base site pairs has been well established.[2] The reaction begins with an initial keto–enol tautomerization of the aldehyde.[15] First, an aldehyde encounters the acid–base site pair, during which the proton transfers to the carbonyl oxygen of the aldehyde, whereas the neighboring framework oxygen attacks its alpha hydrogen, forming an enol.[16] The enol then attacks a vicinal, protonated aldehyde in a step that

[a] Dr. Y. Yang, F. Lin, Prof. H. Tran, Prof. Y.-H. Chin
Department of Chemical Engineering and Applied Chemistry
University of Toronto
Toronto, Ontario, M5S 3E5 (Canada)
Fax: (+)416 978 8605
E-mail: cathy.chin@utoronto.ca

Supporting information and the ORCID identification number(s) for the author(s) of this article can be found under http://dx.doi.org/10.1002/cctc.201601042.

creates the intermolecular C–C bond and forms a hydroxyl–aldehyde intermediate, which upon sequential dehydration evolves a larger, unsaturated aldehyde as the condensation product.[15] The unsaturated aldehyde could also coordinate to the H^+ site as a hydrogen-bonded complex. The aldol condensation occurs in parallel with transfer hydrogenation and dehydration that form alkene and diene, respectively.[2] All three primary reactions occur concomitantly at the catalyst surfaces and their rates depend on the coverages and identity of the reaction intermediates. For this reason, we seek to understand the interactions between aldehydes and solid Brønsted acid sites, probe the kinetic significance of the various aldehyde-derived species, and relate these species to the various catalytic events during aldehyde deoxygenation reactions.

Polyoxometalate clusters are a class of solid acid catalysts with well-defined Keggin structure and chemical compositions of $H^+_{8-n}[X^{n+}Y_{12}O_{40}]^{n-8}\cdot zH_2O$ (with X = P, Si, or B; Y = Mo, W, or V; n = oxidation state of X, z = 0–8). Their precise atomic connectivity allows the accurate tuning of their acid strength and site concentrations, by varying the identity of the central atoms (X) or substituting their protons (H^+) with other cations (e.g., Na^+, K^+), while maintaining the overall structural integrity. They are effective catalysts for the deoxygenation of light oxygenates, as reported for 1,2-propylene glycol dehydration on $H_4SiW_{12}O_{40}$,[17] glycerol dehydration on $H_3PMo_{12}O_{40}$ and $H_3PW_{12}O_{40}$ clusters,[17,18] and 2-butanol dehydration on $H_{8-n}X^{n+}W_{12}O_{40}$ (X = P, Si, Al, and Co) clusters.[19] Their structures also do not impose local, molecular scale confinements on the active sites, thus eliminating the effects arising from van der Waals interactions prevalent in acidic, microporous crystalline solids. These structural and compositional flexibilities (of polyoxometalate clusters) and their lack of local confinements have allowed detailed, rigorous assessments of kinetics and their connection to the acid strength, as demonstrated previously for the case of 2-butanol dehydration.[19] Their lack of local site confinements promotes the aldol condensation much more effectively while suppressing hydride transfer and dehydration reactions that form light alkenes and alkadienes, relative to microporous crystalline catalysts (H-ZSM-5 and H-FAU zeolites). For example, the overall carbon selectivity to butene and butadiene is approximately 3% on $H_4SiW_{12}O_{40}$, much less than the 40% on H-MFI and 38% on H-FAU during butanal reactions at 573 K (space velocity: 0.045, 0.0033, and 0.0074 s^{-1} on $H_4SiW_{12}O_{40}$, H-MFI, and H-FAU, respectively).[20] For these reasons, polyoxometalate clusters are an important class of catalysts for selective transformation of small aldehydes to larger, more valuable oxygenates.

Previous kinetic studies[21] have shown that polyoxometalate clusters are selective for aldol condensation, but the details of aldehyde adsorption and activation remain unestablished. Here, we probe the adsorption and activation of butanal, a model compound of aldehydes, on $H_xNa_{4-x}SiW_{12}O_{40}$ (x = 0–4) and $H_yNa_{3-y}PW_{12}O_{40}$ (y = 0–3) polyoxometalate clusters, with different site densities using combined IR spectroscopic and kinetic studies. Our findings show that butanals initially adsorb on the H^+ sites as H^+-bonded complexes (RC=O···H^+), a portion of which converts to surface acetate by reactions with a vicinal framework oxygen atom and remains as spectators during catalysis. The other portion of H^+-bonded butanals undergoes aldol condensation to produce 2-ethyl-2-hexenal, which may undergo sequential condensation and cyclization–dehydration, leading to cyclic oxygenates or aromatics. On Na^+ sites, butanals adsorb onto the Na^+ sites as inactive Na^+-bonded complexes (RC=O···Na^+) and these complexes do not participate in the reactions. These systematic studies on the adsorbed species and their catalytic roles shed light into the catalytic details and the connection between site structures and their rates and selectivities.

Results and Discussion

Quantifications of Brønsted and Lewis acid sites on supported $H_xNa_{4-x}SiW$ and $H_yNa_{3-y}PW$ clusters by pyridine adsorption and temperature-programmed desorption (TPD)

A series of $H_xNa_{4-x}SiW_{12}O_{40}$ (x = 0–4) or $H_yNa_{3-y}PW_{12}O_{40}$ (y = 0–3) polyoxometalate clusters supported on SiO_2 with varying densities of Brønsted and Lewis acid sites are synthesized according to the methods described in Experimental Section. $H_xNa_{4-x}SiW_{12}O_{40}$ (x = 0–4) or $H_yNa_{3-y}PW_{12}O_{40}$ (y = 0–3) polyoxometalate clusters are denoted hereinafter as $H_xNa_{4-x}SiW$ (x = 0–4) and $H_yNa_{3-y}PW$ (y = 0–3), respectively. Butanal titrations at 348 K show that most of the H^+ and Na^+ sites remain accessible to butanal molecules, with near unity butanal-to-cation ratios (0.78 to 0.96 on $H_xNa_{4-x}SiW$ and 0.84–0.98 on $H_yNa_{3-y}PW$, respectively, Table 1). A very small portion of the H^+ and Na^+ sites is inaccessible to the titrant, likely because of cluster aggregation. IR absorption spectra for pyridine adsorption on the series of $H_xNa_{4-x}SiW$ (x = 0–4) and $H_yNa_{3-y}PW$ (y = 0–3) samples are shown in Figures 1a and 1b, respectively, with varying Brønsted acid site densities, χ_i [Eq. (8), in Experimental Section], at 348 K, together with a spectrum for pyridine adsorption on bare SiO_2 (without polyoxometalate clusters, in Figure 1b) as the reference. The absorption bands at 1637 cm^{-1}, 1540 cm^{-1}, and 1490 cm^{-1} correspond to the Py–H^+ stretching (Py denotes pyridine) of pyridinium ions adsorbed at the Brønsted acid sites (H^+)[22] and the bands at 1611 cm^{-1}, 1490 cm^{-1}, and 1450 cm^{-1} to Py–L stretching (L denotes Lewis acid site) of pyridine coordinatively bonded to Lewis acid sites of polyoxometalate clusters.[22b] Pyridine adsorption on bare SiO_2 leads to bands at 1595 cm^{-1} and 1445 cm^{-1}, which correspond to the binding of pyridine at weak Lewis acid sites at SiO_2 surfaces. These peaks associated with SiO_2 disappear after dispersing the polyoxometalate clusters onto SiO_2 surfaces, caused apparently by the occupation of these sites by the clusters.

Pyridine uptakes on the series of samples were determined from separate pyridine chemical titrations (in flow mode) at 473 K, during which pyridine was introduced to and adsorbed onto the catalysts. The cumulative pyridine uptakes for each polyoxometalate cluster [λ_{ads}, Eq. (9)] reflect the amounts of pyridine adsorbed per cluster at saturation. These uptakes are summarized in Table 1. After the titration experiments, the overall amounts of pyridine desorbed from the catalysts [$\lambda_{des,overall}$, Eq. (11)] were measured from the sequential tempera-

Table 1. Nominal H^+ site densities and pyridine/butanal uptakes on $H_xNa_{4-x}SiW$ ($x=0$–4) and $H_yNa_{3-y}PW$ ($y=0$–3) clusters.

Sample	Nominal H^+ (χ_i, i = Si,P) [mol mol$_{cluster}^{-1}$]	Pyridin uptake (λ_{ads}) [mol mol$_{cluster}^{-1}$]	Pyridine desorption during TPD experiments [mol mol$_{cluster}^{-1}$]				Butanal uptake (α_{but}) [mol mol$_{cluster}^{-1}$]	Butanal-to-cation ratio
			Total ($\lambda_{des,overall}$)[a]	Low ($\lambda_{des,1}$)[b]	Medium ($\lambda_{des,2}$)[c]	High ($\lambda_{des,3}$)[d]		
H_4Na_0SiW	4	3.13	2.72	0.92	1.49	0.31	3.33	0.83
H_3Na_1SiW	3	2.63	2.55	0.83	1.46	0.27	3.30	0.82
H_2Na_2SiW	2	1.86	1.39	0.36	0.90	0.13	3.85	0.96
H_1Na_3SiW	1	1.07	0.82	0.28	0.54	B.D.	3.43	0.86
H_0Na_4SiW	0	0.93	0.51	0.51	B.D.	B.D.	3.10	0.78
H_3Na_0PW	3	2.68	2.12	0.28	1.57	0.27	2.93	0.98
H_2Na_1PW	2	1.70	1.67	0.36	1.08	0.23	2.62	0.87
H_1Na_2PW	1	1.22	0.96	0.54	0.42	B.D.	2.53	0.84
H_0Na_3PW	0	0.98	0.77	0.77	B.D.	B.D.	2.64	0.88

[a] Obtained by integrating the pyridine desorption peak over the entire temperature range; [b], [c], and [d] obtained by decoupling the pyridine desorption peak to three temperature ranges of 500–650 K, 550–750 K, and 673–790 K, respectively; B.D.: below the detectable limit.

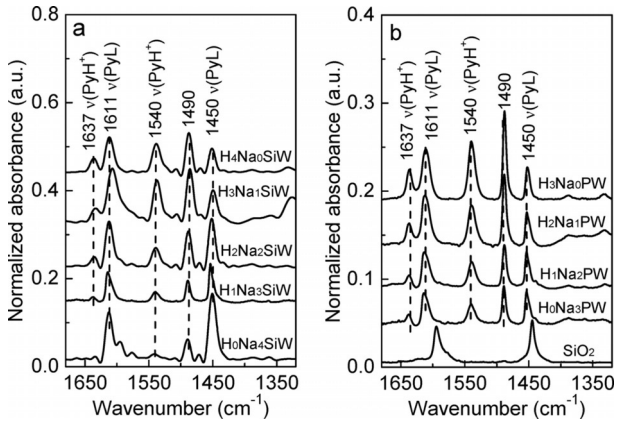

Figure 1. Normalized IR absorption spectra taken after pyridine adsorption (0.88–1.32 μmol) on (a) $H_xNa_{4-x}SiW$ ($x=0$–4) and (b) $H_yNa_{3-y}PW$ ($y=0$–3) at 473 K and then cooling to 348 K for measurements.

ture-programmed desorption (TPD) experiments and are also summarized in Table 1. The uptake values λ_{ads}, which reflect the molar ratio of pyridine per polyoxometalate cluster, are 3.13 for H_4Na_0SiW and 2.68 for H_3Na_0PW clusters. Exchanging a portion of the H^+ sites with Na^+ ions in $H_xNa_{4-x}SiW$ decreased the nominal H^+ site densities [χ_i, Eq. (8)] from 4 to 0 and the related λ_{ads} values from 3.13 to 0.93. Similarly, exchanging the H^+ with Na^+ on $H_yNa_{3-y}PW$ decreased the nominal H^+ densities from 3 to 0 and in turn the λ_{ads} values from 2.68 to 0.98.

Pyridine desorption rates during TPD from the series of $H_xNa_{4-x}SiW$ ($x=0$–4) and $H_yNa_{3-y}PW$ ($y=0$–3) clusters are shown in Figures 2a and 2b, respectively. These desorption rates reflect strictly the contributions from the polyoxometalate clusters, free of those from SiO_2 supports, because He purge at 473 K for 30 min, conducted before the temperature-programmed experiments, removed all weakly adsorbed pyridines on SiO_2 surfaces. In addition, pyridine desorption peaks in the TPD profiles are ascribed to those adsorbed on the Brønsted acid sites only, because most of the pyridines adsorbed on the Lewis acid sites (1450 cm^{-1}) were easily removed, either by purging with flowing He (Figure S1) or by evacuating (Figure S2) the samples at 473 K. There are only a small amount of strong Lewis sites which can bind to pyridines. This is supported by our previous study in which the Brønsted-to-Lewis acid site ratio on H_4Na_0SiW sample was determined to be approximately 15:1, based on the IR spectra of pyridine adsorption followed by He purging.[21]

On both sample series, pyridine desorption began at similar temperatures (≈500 K), irrespective of their H^+ site densities [χ_i, i = Si or P, Eq. (8)] and the identity of the central atom (Si or P). Pyridine desorption, however, completed at temperatures that varied with the H^+ site densities [χ_i, Eq. (8)], if comparing within the same series of either $H_xNa_{4-x}SiW$ or $H_yNa_{3-y}PW$ clusters. Pyridine desorbed from these samples in three different temperature ranges of 500–650 K, 550–750 K, and 673–790 K. Our previous study shows that thermal treatment at 673 K may reduce the H^+ site densities on $H_3PW_{12}O_{40}$ (by 17%) through dehydration.[21] Notably, the pyridine desorption above 673 K occurs together with a concomitant reduction in the H^+ site

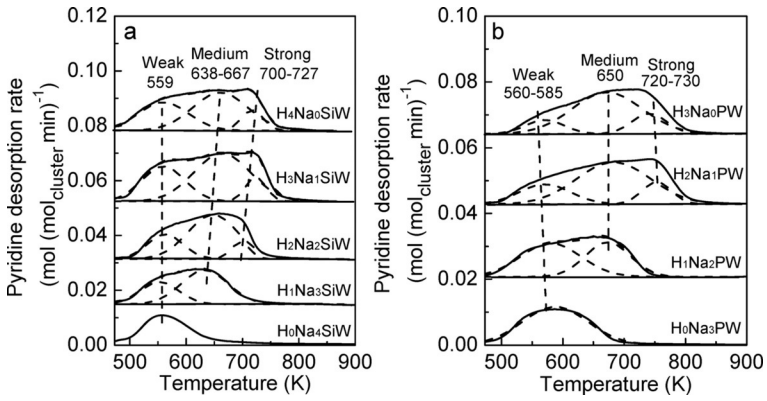

Figure 2. Pyridine desorption rates during TPD of pyridine on (a) $H_xNa_{4-x}SiW$ ($x=0$–4) and (b) $H_yNa_{3-y}PW$ ($y=0$–3), after pyridine adsorption followed by purging in flowing He for 30 min at 473 K (heating rate = 0.033 K s^{-1}).

density, as the Keggin clusters dehydrate while maintaining their structural integrity.[23] The decomposition of polyoxometalate clusters (into WO_3 and SiO_2[23]) takes place above approximately 800 K, according to the thermogravimetric–differential scanning calorimetric analyses (TG–DSC) of $H_4SiW_{12}O_{40}$ catalysts in our previous work.[21] The onset temperature of decomposition is consistent with those previously reported one based on differential thermal analyses (DTA) and X-ray diffraction (XRD) analyses (803 K for $H_4SiW_{12}O_{40}$ and 773 K for $H_3PW_{12}O_{40}$).[23] Since most pyridine molecules desorb below 800 K (Figure 2), the pyridine TPD profiles reflect mostly the binding strengths of pyridine molecules on the intact clusters.

It has been established that H^+ sites on the polyoxometalate clusters are chemically equivalent to each other[24] and their acid strengths are dictated by the enthalpies required to remove them to noninteracting distances from the clusters, as defined by the deprotonation enthalpy (ΔH_{DPE}, which equals the heat of reaction for $H_nXY_{12}O_{40} \rightarrow H^+ + H_{n-1}XY_{12}O_{40}^-$; X = P, Si, or B, Y = Mo, W, or V, n = oxidation state of X; ΔH_{DPE} values are 1087 kJ mol^{-1} for $H_3PW_{12}O_{40}$ and 1105 kJ mol^{-1} for $H_4SiW_{12}O_{40}$ clusters).[19a,25] However, if a portion of the H^+ sites on a cluster was partially replaced by Na^+ ions or was occupied by pyridines (as $C_5H_5NH^+$), the deprotonation enthalpies for the remaining H^+ sites would increase and acid strength would commensurately decrease. Na^+ and pyridinium ion ($C_5H_5NH^+$) have lower electron affinities (496[26] and 590 kJ mol^{-1},[27] respectively) than H^+ (1312 kJ mol^{-1}).[26] Thus, replacing H^+ sites by Na^+ ions or adsorbing pyridine onto the H^+ sites, transforming them into $C_5H_5NH^+$ ions, would result in less extent of charge delocalization on polyoxometalate anions ($SiW_{12}O_{40}^{4-}$ and $PW_{12}O_{40}^{3-}$) to these cations. The lower extent of delocalization causes the anions to bind to the remaining H^+ sites more strongly. We hypothesize that this extent of charge delocalization leads to the multiple desorption peaks during the TPD (Figure 2): during the desorption of a pyridine (C_5H_5N) molecule, the pyridinium ion ($C_5H_5NH^+$) converts back to a H^+ ion, which interacts with the anion more strongly than for the case of $C_5H_5NH^+$ ion–anion interactions. This increase in the anion–H^+ interactions decreases the extent of electron donation from the anion to the rest of the H^+ ions and thus causes the strength of the remaining H^+ sites on the polyoxometalate clusters to increase concomitantly. Such changes in acid strength lead to the higher desorption temperature required for the removal of next pyridine molecules from the polyoxometalate clusters. For the Na^+ exchanged samples, the anion–Na^+ interactions are weaker than the anion–H^+ interactions. As a result, the anion retains most of its negative charge and is able to donate the electron density into the remaining H^+ sites, making them weaker. These weaker H^+ sites give the pyridine desorption peak at the lower temperatures.

Pyridine also desorbs from H-Beta and H-ZSM-5 zeolites at similar temperature ranges,[28] on which H^+ sites are weaker and deprotonation enthalpies are higher at 1195 kJ mol^{-1} and 1200 kJ mol^{-1},[25] respectively. Pyridine desorbs from H-Beta (Si/Al = 13) in the temperature ranges of 453–623 K, 473–873 K, and 673–1023 K and from H-ZSM-5 (Si/Al = 84) in the ranges of 423–573 K and 673–973 K. The temperature ranges are higher for the zeolites than polyoxometalate clusters (Figure 2), likely because the heats of pyridine desorption (ΔH_{des}, which reflect the heats of reaction for $PyH^+ \rightarrow Py + H^+$) in these microporous crystalline structures (5.6 Å and 6.6–7.7 Å for H-beta and 5.5 Å for H-ZSM-5) contain significant enthalpy contributions arising from van der Waals interactions between pyridines and the local pores and cages of the zeolites.

The overall pyridine desorption rate profiles for $H_xNa_{4-x}SiW$ (x = 0–4) and $H_yNa_{3-y}PW$ (y = 0–3) in Figure 2 were decoupled into three temperature ranges of 500–650 K, 550–750 K, and 673–790 K and their corresponded amounts of pyridine desorbed, denoted as $\lambda_{des,1}$, $\lambda_{des,2}$, and $\lambda_{des,3}$ [Eq. (10)], are summarized in Table 1. Within each series of samples, both the total amount of pyridine desorbed [$\lambda_{des,overall}$, Eqs. (11) and (12)] and the amount of pyridine desorbed at the higher temperatures ($\lambda_{des,2-3}$) increase linearly with the nominal H^+ site densities [χ_i, Eq. (8)], as shown in Figure 3a. The dotted lines in Figure 3a

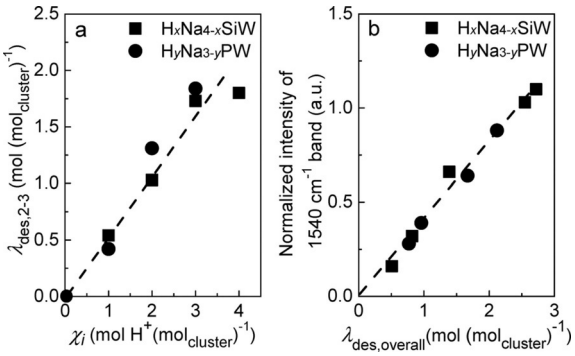

Figure 3. (a) The total amount of pyridine desorbed ($\lambda_{des,overall}$, between 500–790 K) [Eq. (11)] and the amount of pyridine desorbed from the high temperature ranges ($\lambda_{des,2-3}$, between 550–790 K) [Eq. (12)] during TPD, plotted as a function of the nominal H^+ site densities (χ_i, i = Si or P) [Eq. (8)] and (b) IR absorption band intensity at 1540 cm^{-1}, which corresponds to pyridinium ion at the Brønsted acid sites, plotted as a function of the overall amount of H^+ sites ($\lambda_{des,overall}$) [Eq. (11)] determined by TPD of pyridine.

are the linear fits for $\lambda_{des,overall}$ and $\lambda_{des,2-3}$; these fits run in parallel, an indication that the last H^+ site on the polyoxometalate clusters is weak (because of the neighboring Na^+ ions), thus it cannot be substituted by a Na^+ ion ($\lambda_{des,1}$, with pyridine desorption temperatures between 500–650 K). The integrated intensities for the pyridine absorption bands at 1540 cm^{-1} and 1450 cm^{-1} in Figure 1 reflect the site densities for Brønsted and Lewis sites,[29] respectively. The integrated intensities at 1540 cm^{-1} increase proportionally with the total amount of pyridine desorbed during TPD [$\lambda_{des,overall}$, Figure 2, Eqs. (11) and (12)] for both $H_xNa_{4-x}SiW$ and $H_yNa_{3-y}PW$ clusters, as shown in Figure 3b, irrespective of the chemical identity of their central atoms. This linear, direct relation suggests that pyridine molecules are desorbed from the Brønsted acid sites during the TPD experiments.

Butanal chemical titration and IR absorption studies on $H_xNa_{4-x}SiW$ ($x=0$–4) and $H_yNa_{3-y}PW$ ($y=0$–3) clusters supported on SiO_2 support

Butanal uptakes determined from chemical titrations performed on the series of $H_xNa_{4-x}SiW$ ($x=0$–4) and $H_yNa_{3-y}PW$ ($y=0$–3) clusters at 348 K give the average number of butanal molecules adsorbed per polyoxometalate cluster, [α_{but}, Eq. (14)], on these samples. The α_{but} values, as summarized in Table 1, are nearly independent of the H^+ densities (χ_i) and the related H^+-to-Na^+ ratios: they range from 3.10 to 3.85 $mol_{butanal}\,mol_{cluster}^{-1}$ for $H_xNa_{4-x}SiW$ clusters and 2.53 to 2.93 $mol_{butanal}\,mol_{cluster}^{-1}$ for $H_yNa_{3-y}PW$ clusters. These α_{but} values suggest that butanal adsorbs on both H^+ and Na^+ sites of the $H_xNa_{4-x}SiW$ and $H_yNa_{3-y}PW$ clusters.

On H_4Na_0SiW and H_3Na_0PW clusters, evacuation under dynamic vacuum (0.01–0.1 mbar) at 348 K after butanal adsorption leads to the IR absorption spectra in Figure 4. The spectra show three regions of: (i) hydroxyl stretching at 3745–3725 cm^{-1} (Figures 4 a,d), (ii) methyl stretching at 3000–2700 cm^{-1} (Figures 4 b,e), and (iii) stretching of adsorbed carbonyl (C=O) and surface acetate (OCO) at 1750–1550 cm^{-1} and methyl bending at 1465–1380 cm^{-1} (Figures 4 c,f). Details of the absorption band assignments are summarized in Table 2, together with those reported in the literature for acetaldehyde adsorption on various oxides (CeO_2[30] and TiO_2)[31] and zeolites (H-ZSM-5[9] and Na-Y).[32] Butanal adsorption on polyoxometalate clusters leads to the detection of C=O stretching vibration [$\nu_{but.}$(C=O)] at approximately 1707 cm^{-1} (Figures 4 c,f) through binding its carbonyl oxygen on the Brønsted acid site (H^+) as a RC=O···H^+ complex (Structure **A,** Scheme 1),[9] which causes a red-shift of approximately 43 cm^{-1} from that of its gas-phase molecule (Table 2). This shift is a result of the partial proton transfer to the carbonyl group, which polarizes and weakens the C=O bonds of the adsorbed butanal.[10c,16]

The bands at 1654 cm^{-1} [$\nu_{di.}$(C=O)] and 1632 cm^{-1} [ν(C=C)] are indicative of adsorbed 2-ethyl-2-hexenal, the aldol condensation product,[30] as it interacts with the H^+ site through its carbonyl oxygen atom (Structure **B**, Scheme 1). The bands detected at 1580 cm^{-1} on H_4Na_0SiW (Figure 4 c) and 1577 cm^{-1} on H_3Na_0PW (Figure 4 f) suggest the formation of surface acetate [ν_{as}(OCO), Structure **C**, Scheme 1], as found also during acetaldehyde adsorption on oxide surfaces (CeO_2[30] and TiO_2).[31] Acetaldehyde adsorption at 473 K led to the characteristic surface acetate band at 1542 cm^{-1} on CeO_2 and at 1562 cm^{-1} on TiO_2.[30,31] The coverages of surface acetate are determined from the ν_{as}(OCO) band intensities at 1580 and 1577 cm^{-1} for the entire series of $H_xNa_{4-x}SiW$ ($x=0$–4) and

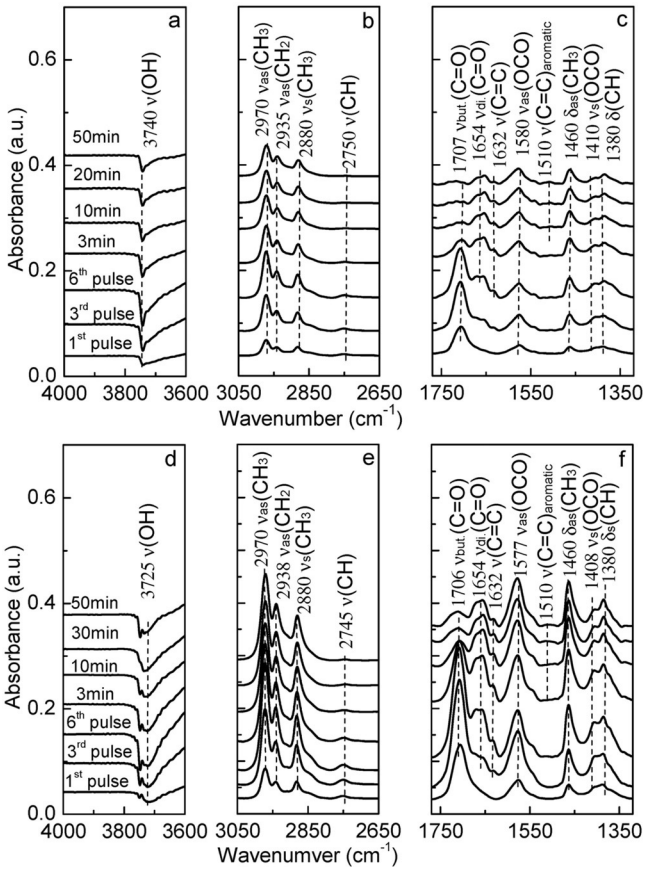

Figure 4. IR absorption spectra, taken during adsorption of butanal (6 pulses total, 0.32 μmol per pulse, labeled 1st, 3rd, and 6th pulse) to saturation coverages and then evacuation under dynamic vacuum at 348 K, on (a,b,c) H_4Na_0SiW and (d,e,f) H_3Na_0PW clusters. The evacuation times (3–50 min) are indicated. Region (a, d) 3600–4000 cm^{-1} corresponds to the region of hydroxyl stretching, Region (b, e) 2650–3050 cm^{-1} to methyl stretching, and Region (c, f) 1320–1770 cm^{-1} to carbonyl stretching, surface acetate stretching, and methyl bending, respectively.

Table 2. IR absorption band (in cm^{-1}) assignments for butanal adsorption on $H_xNa_{4-x}SiW$ ($x=0$–4) and $H_yNa_{3-y}PW$ ($y=0$–3) clusters at 348 K and acetaldehyde adsorption on oxides and zeolites at 313 K.

Band	C_4H_8O (g)[a]	H_4Na_0SiW	H_0Na_4SiW	H_3Na_0PW	H_0Na_3PW	CeO_2 [30]	TiO_2 [31]	Na-Y[32]	H-ZSM-5[9]
$\nu_{as}(CH_3)$	2972–2894	2970–2935	2970–2935	2970–2935	2970–2935	2960	2969	3050	–
$\nu_s(CH_3)$	2805	2880	2880	2880	2880	–	2914	–	–
ν(CH)	2710	2750	2754	2745	2750	2727	2759	2750	–
$\nu_{but.}$(C=O)	1750	1707	1720	1706	1715	1729	1718	1722	1707
$\nu_{di.}$(C=O)	–	1654	1690	1654	1690	1686	1686	-	1630
ν(C=C)	–	1632	–	1632	–	–	1636	–	1602
ν_{as}(OCO)	–	1580	–	1577	–	1542	1562	–	–
ν(C=C)$_{aromatic}$	–	1510	–	1510	–	–	–	–	–
$\delta(CH_3)$	1462–1394	1460–1380	1460–1380	1460–1380	1460–1380	1440–1372	1355	1428–1349	1430–1397

[a] IR spectrum of gas phase butanal was measured at room temperature and shown in Figure S3.

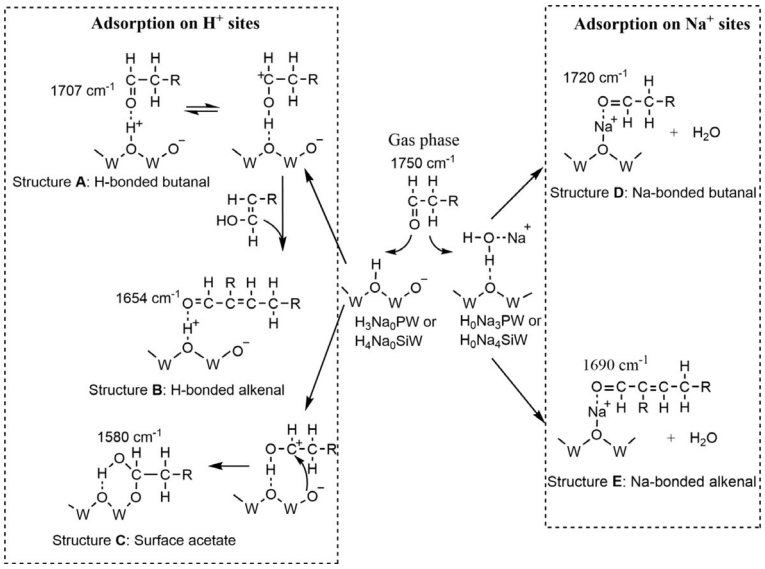

Scheme 1. Adsorption configurations of butanal on $H_xNa_{4-x}SiW$ ($x=0$–4) and $H_yNa_{3-y}PW$ ($y=0$–3) clusters. R denotes the $-CH_2-CH_3$ group. The wavenumbers corresponding to the carbonyl and acetate group stretching are indicated.

preferential adsorption and protonation of aldehydes on H^+ sites have been previously confirmed from butanal titration, which gives C_4H_8O/H^+ molar ratios of 1.0, 1.01, and 1.1 on MFI (348 K), H-FAU (448 K), and $H_4SiW_{12}O_{40}$ (348 K),[20] respectively, and consistent with the first-order rate dependence for the primary, propanal aldol condensation rates with propanal pressure.[2] An adjacent lattice oxygen (O_{ox}, Lewis basic site) acting as a nucleophile attacks the carbonyl carbon of the protonated butanal, resulting in the adsorbed acetate ($C_4H_8O-H^+-O_{ox}$, Structure **2.2**),[33] as depicted in Scheme 2. The H^+ and vicinal lattice oxygen (O_{ox}) acting as a Brønsted acid–base site pair; the site pair catalyzes several classes of reaction, such as acetaldehyde keto–enol tautomerization on ZSM-5[15] and butanol dehydration on $H_{8-n}X^{n+}W_{12}O_4$ (X = P, Si, Al, and Co) polyoxometalate clusters.[19a] The surface acetate species remain stable only at low temperatures (< 348 K) and easily desorb to evolve into heavy aromatics during the sequential heating stage, as evidenced from the

$H_yNa_{3-y}PW$ ($y=0$–3) clusters, respectively, as shown in detail in Figures 7 c,f. The ν_{as}(OCO) band intensities appear to relate directly to the amount of pyridine desorbed between 673–790 K during the TPD of pyridine [$\lambda_{des,3}$ Eq. (10)], as depicted in Figure 5. The linear relation between the results from two independent characterization techniques, that is, the IR absorption band intensities for surface acetate at 1580 cm^{-1} or 1577 cm^{-1} and the amounts of pyridine desorbed from 673–790 K during the TPD experiments, confirms that both the surface acetates and the strongly chemisorbed pyridine molecules preferentially occupy an identical type of sites. Such relation appears to remain so, irrespective of the chemical identity of the central atom of polyoxometalate clusters.

The surface acetate formation may involve an initial butanal protonation which forms the $C_4H_8O-H^+$ (Structure **2.1**, Scheme 2) as the most abundant surface intermediate. The

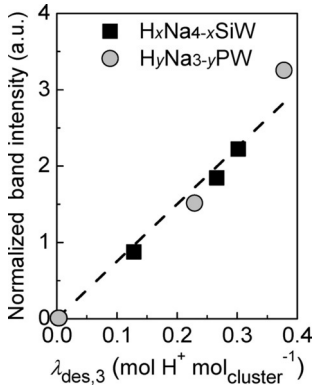

Figure 5. Normalized IR absorption band intensities of surface acetate (1580 cm^{-1} for $H_xNa_{4-x}SiW$ and 1577 cm^{-1} for $H_yNa_{3-y}PW$ clusters), plotted as a function of the H^+ site densities determined during TPD of pyridine between 673 K and 790 K [$\lambda_{des,3}$, Eq. (10)].

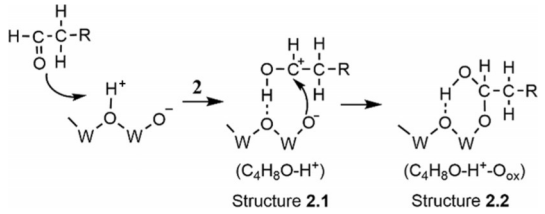

Scheme 2. Proposed pathway for surface acetate formation on $H_xNa_{4-x}SiW$ ($x=2$–4) and $H_yNa_{3-y}PW$ ($y=2$–3) clusters during butanal adsorption at 348 K.

changes in the ν_{as}(OCO) band (at 1580 cm^{-1}) on H_4Na_0SiW clusters to the $\nu(C=C)_{aromatic}$ band (1600 cm^{-1}) in Section S4 of Supporting Information. This finding is in line with our previous work, in which we have demonstrated that only cokes but no acetate species remain on the H_4Na_0SiW clusters after butanal reactions at high temperatures (523–573 K) and that the coke formation poisons all the strong H^+ sites and a portion of medium and weak H^+ sites.[21]

Butanal adsorption and the formation of adsorbed 2-ethyl-2-hexenal and surface acetate (OCO) at the Brønsted acid sites perturb the hydroxyl stretching bands at 3740 cm^{-1} on H_4Na_0SiW and 3725 cm^{-1} on H_3Na_0PW clusters, as evidenced by the appearance of negative absorption bands in Figures 4 a,d. These events also lead to the series of bands at 2754–2970 cm^{-1}, which correspond to the different modes of methyl stretching from the adsorbed butanal, 2-ethyl-2-hexenal, and surface acetate (Structures **A**, **B**, and **C**, respectively, in Scheme 1), and the concomitant evolvement of bands related to their bending vibrations in 1500–1350 cm^{-1} in Figure 4. The intensities of these bands, including hydroxyl stretching [ν(OH)] at 3740 cm^{-1} and 3725 cm^{-1}, methyl stretching [$\nu(CH_3)$] at 2754–2970 cm^{-1}, carbonyl stretching [ν(C=O)] at 1707 cm^{-1} and 1654 cm^{-1}, acetate stretching [ν_{as}(OCO)] at 1580 cm^{-1} and

1577 cm^{-1}, and methyl bending [$\delta(CH_3)$] at 1500–1350 cm^{-1}, initially increased as the exposure to butanal increased (Figure 4, labeled 1st, 3rd, and 6th pulses, each with 0.32 μmol of butanal). Above a threshold butanal exposure, the band intensities became unchanged because the surface reached saturation. Sequential evacuation under dynamic vacuum at 348 K removed the butanal molecules (Structure **A**, Scheme 1) selectively, as shown from the marked decrease in the band intensities for the C=O vibration of butanal at approximately 1707 cm^{-1} in Figures 4c,f. In contrast, band intensities related to the adsorbed 2-ethyl-2-hexenal [e.g., the ν(C=O) at 1654 cm^{-1} and ν(C=C) at 1632 cm^{-1}] and surface acetate [ν_{as}(OCO) at 1580 cm^{-1} or 1577 cm^{-1}] remained relatively stable at 348 K for the entire evacuation period (50 min) under dynamic vacuum, as shown in the same profiles in Figure 4. During the evacuation, a band at 1510 cm^{-1}, which corresponds to the C=C stretching in light aromatics [$\nu(C{=}C)_{aromatic}$], began to emerge at approximately 10 min. This band reflects the formation of aromatics from the sequential condensation, ring-closure, and dehydration reactions of alkenals,[1b,2] as described below.

Isothermal butanal adsorption at 348 K on H_0Na_4SiW and H_0Na_3PW clusters, which contain predominantly Na^+ ions with a small fraction of residue H^+ sites [$\lambda_{des,overall}$, Eq. (11), residue H^+ site densities of 0.51 and 0.77 mol $mol_{cluster}^{-1}$, respectively] gives absorption spectra unlike those of the fully protonated H_4Na_0SiW and H_3Na_0PW clusters. The spectra of adsorbed butanal, taken under dynamic vacuum and shown in Figure 6, show absorption bands at 1720–1715 cm^{-1} on both H_0Na_4SiW and H_0Na_3PW clusters. These bands, undetected on H_4Na_0SiW and H_3Na_0PW clusters (Figure 4), reflect the formation of butanal–Na^+ complex [$RCH_2(CH{=}O)\cdots Na^+$ complex, Structure **D**, Scheme 1] with a red-shift of approximately 30 cm^{-1} from that of the gas-phase butanal (Table 2). The shift may reflect electron transfer from the carbonyl groups to polyoxometalate frameworks and thus the weakening of the C=O bonds in butanals.[14] The new feature emerged at 1690 cm^{-1} may reflect the C=O vibrational band of 2-ethyl-2-hexenal, formed from the aldol condensation reactions on H^+ sites and migrated to bond to the Na^+ sites (Structure **E**, Scheme 1). The Na^+ sites are inactive in catalyzing the aldol condensation, as confirmed in our previous work on butanal reaction on Na^+ exchanged MFI zeolites at 573 K.[20] The negative peak at 1625 cm^{-1}, which corresponds to the bending vibration of water, emerged because skeleton water was eliminated from the H_0Na_4SiW and H_0Na_3PW clusters as butanal adsorbed,[34] as these clusters contained crystal water even after the initial pretreatment.[35] In the hydroxyl region (Figures 6a,d), a trace amount of butanal adsorbed on the silanol group of SiO_2 supports and led to the weak negative peak at 3745 cm^{-1}. The assignment of this peak was confirmed from IR absorption experiments of butanal adsorption on bare SiO_2 support, also shown in Figure 7d.

The IR absorption spectra for butanal adsorption on the series of $H_xNa_{4-x}SiW$ (x=0–4) and $H_yNa_{3-y}PW$ (y=0–3) clusters with different H^+ site densities [χ_i, Eq. (8)] and therefore different Na^+ site densities are shown Figure 7, taken under dynamic vacuum at 348 K. The H^+ densities are related to the Na^+

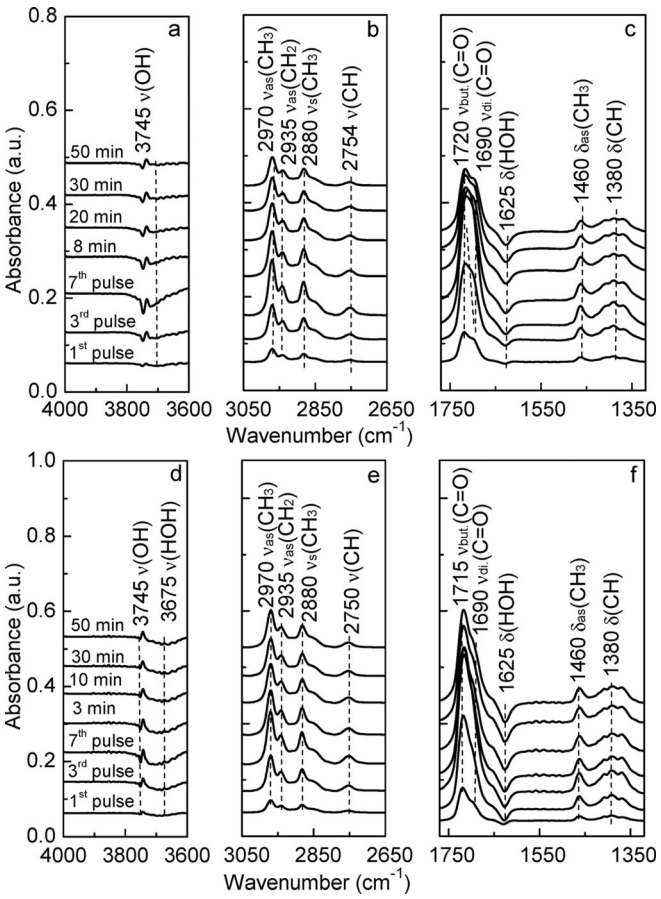

Figure 6. IR absorption spectra, taken during adsorption of butanal (7 pulses total, 0.32 μmol per pulse, labeled 1st, 3rd, and 7th pulse on the Figure) to saturation coverages and then evacuation under dynamic vacuum, on (a,b,c) H_0Na_4SiW clusters and (d,e,f) H_0Na_3PW clusters at 348 K. The evacuation times are provided. Region 3600–4000 cm^{-1} (a,d) corresponds to the region of hydroxyl stretching, Region 2650–3050 cm^{-1} (b,e) to methyl stretching, and Region 1320–1770 cm^{-1} (c,f) to carbonyl stretching, surface acetate stretching, and methyl bending.

site densities, because the sum of site densities (both H^+ and Na^+) equals 4 for $H_xNa_{4-x}SiW$ (x=0–4) and 3 for $H_yNa_{3-y}PW$ (y=0–3) clusters, as required by the overall site balance relation. Butanal adsorption on both series of $H_xNa_{4-x}SiW$ and $H_yNa_{3-y}PW$ clusters with high H^+ site densities ($\chi_i > 2$) leads to the formation of surface acetate [ν_{as}(OCO) at 1580 cm^{-1} or 1577 cm^{-1}, Figures 7c and 7f]. As the nominal H^+ density [χ_i, Eq. (8)] decreases and the Na^+ density concomitantly increases, the δ(HOH) peak at 1625 cm^{-1} gradually increases because more butanals adsorb at the Na^+ sites. This decrease in the nominal H^+ site density (χ_i) leads also to the decrease in the ν_{as}(OCO) band intensity and the concomitant increase in the $\nu_{but.}$(C=O) band intensity. The disappearance of the ν_{as}(OCO) band indicates that surface acetate forms only at the H^+ site and not at the Na^+ site. If the nominal H^+ site density (χ_i) varies, the $\nu_{di.}$(C=O) bands corresponding to 2-ethyl-2-hexenal remain unchanged, as shown in Figure S6. In addition, the characteristic C=O stretching bands for adsorbed butanal shift from ≈1706 cm^{-1} (bound on H^+ sites) to ≈1720 cm^{-1} (bound on Na^+ sites) for both $H_xNa_{4-x}SiW$ (x=0–4) and $H_yNa_{3-y}PW$ (y=

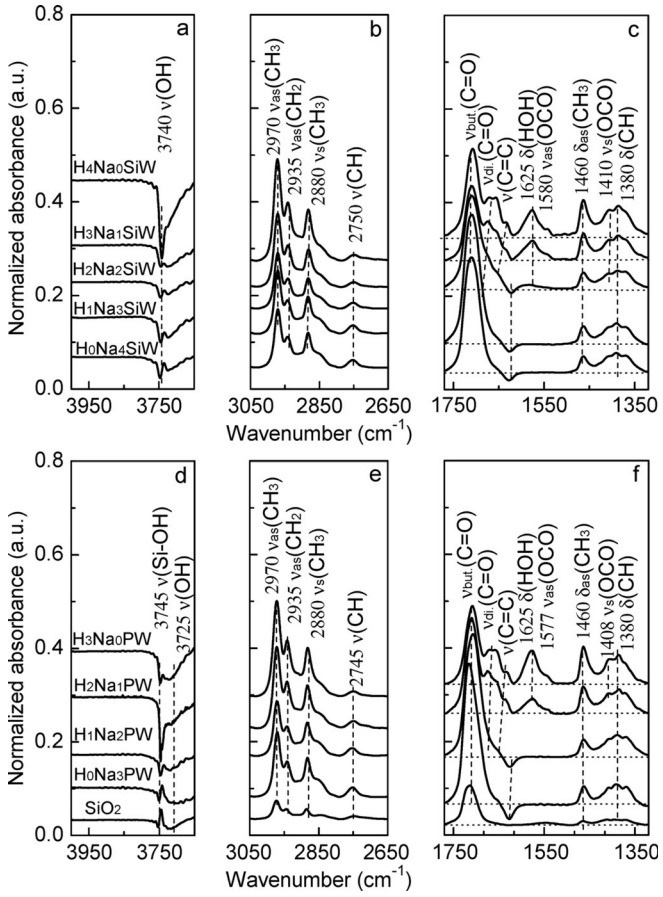

Figure 7. IR absorption spectra, taken during evacuation under dynamic vacuum at 348 K, after butanal adsorption on (a,b,c) $H_xNa_{4-x}SiW$ clusters ($x=0$–4) and (d,e,f) $H_yNa_{3-y}PW$ clusters ($y=0$–3) to surface saturation. Region 3600–4000 cm^{-1} (a,d) corresponds to the region of hydroxyl stretching, Region 2650–3050 cm^{-1} (b,e) to methyl stretching, and Region 1320–1770 cm^{-1} (c,f) to carbonyl stretching, surface acetate stretching, and methyl bending.

0–3) clusters with decreasing H^+ site density. Similarly, the vibrational frequencies of the $\nu_{di.}(C=O)$ bands of adsorbed 2-ethyl-2-hexenal [for example, 1654 cm^{-1} for H_4Na_0SiW clusters] also shift to higher wavenumbers. These changes in wavenumbers reflect the decreasing extent of interactions between the cation (H^+ or Na^+) and the carbonyl groups.

Rates and selectivities of butanal deoxygenation on supported $H_xNa_{4-x}SiW$ and $H_yNa_{3-y}PW$ clusters

The reaction pathways for butanal deoxygenation on $H_xNa_{4-x}SiW$ ($x=0$–4) and $H_yNa_{3-y}PW$ ($y=0$–3) clusters proposed in Scheme 3 are consistent with those proposed for butanal reactions on H-FAU and H-MFI[20] and also for propanal reactions on H-MFI.[2] Polyoxometalate clusters catalyze butanal deoxygenation via stepwise intermolecular C=C bond formation (steps a1–a3) as the predominant reaction path (>80% carbon selectivities). The series of reactions occurs at H^+ sites through the initial attack of protonated butanal by another butanal in its tautomeric form (butenol). These coupling reactions repeat multiple times and lead to a systematic increase in its molecular size from butanal (C_4) to 2-ethyl-2-hexenal (C_8), 2,4-diethyl-2,4-octadienal (C_{12}), 2,4,6-triethyl-2,4,6-decatrienal (C_{16}), and their isomers [e.g., 2-methyl-5-ethyl-cyclopentanone (C_8)], because each intermolecular C=C bond formation event incorporates a butanal unit (four C atoms) into the growing carbon chain and removes a H_2O from the molecule. These reactions produce nearly exclusively oxygenates and aromatics with their carbon numbers equal exactly the multiple of butanal units (C_{4n}, $n=2$, 3, or 4). Unlike butanal reactions on microporous crystalline solids (H-MFI and H-FAU),[20] alkylation/dealkylation reactions of aromatic products remain kinetically inconsequential on polyoxometalate clusters (the aromatic products are almost exclusively C_{4n} species, $n=2$, 3, or 4), because these reactions are prevalent only in pores and cages of molecular dimensions. Polyoxometalate clusters also catalyze the isomerization–dehydration (step b1) and intramolecular C=C bond formation by hydride transfer (step c1) reactions that form butadiene (C_4H_6) and butene (C_4H_8), respectively. These reactions are, however, at least two orders of magnitude smaller than the intermolecular C=C bond coupling ($r_{Intra}/r_{Inter}=0$–0.06, $r_{Dehy}/r_{Inter}=0.008$–0.04, 573 K, as shown by the selectivity data in Table 3). These rate ratios significantly smaller than unity are unlike those found on confined, microporous H-MFI or H-FAU

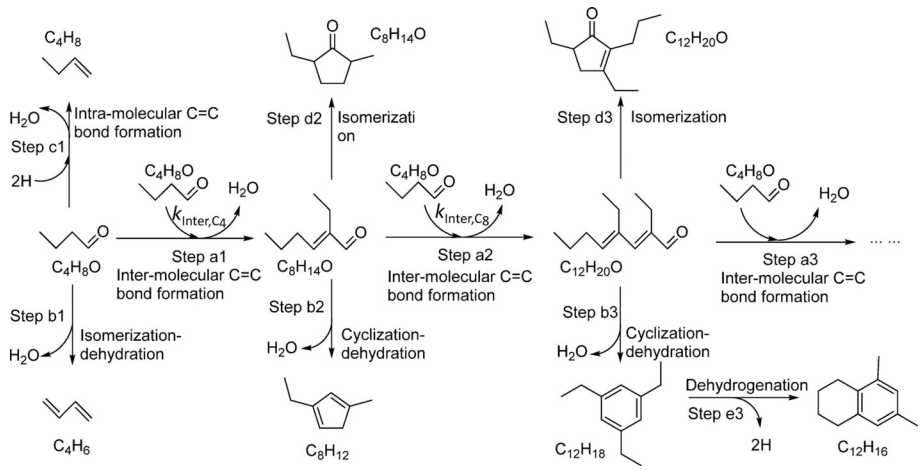

Scheme 3. Reaction pathways for butanal deoxygenation on $H_xNa_{4-x}SiW$ ($x=0$–4) and $H_yNa_{3-y}PW$ ($y=0$–3) clusters.

Table 3. Rate constants and carbon selectivities to various products during butanal deoxygenation on $H_xNa_{4-x}SiW$ and $H_yNa_{3-y}PW$ clusters at 573 K.

Samples	Rate[a] [10^{-3} mol ($mol_{cluster}$ s)$^{-1}$]			Rate constant[c] [10^{-2} mol ($mol_{cluster}$ s kPa)$^{-1}$]		Carbon selectivities in products[e] [mol %]							
						Large alkenals (> C_8)			Large aromatics (> C_8)			C_4 olefin	Other[f]
	r_{Inter}[b]	r_{Dehy}[b]	r_{Intra}[b]	k_{Inter,C_4}[d]	k_{Inter,C_8}[d]	Total	C_8	C_{12-16}	Total	C_8	C_{12-16}		
H_4Na_0SiW	18.2	0.74	0.25	1.95	4.61	83.1	64.6	18.5	14.3	1.6	12.7	2.3	0.3
H_3Na_1SiW	7.5	0.43	0.19	0.76	2.21	82.5	70.0	12.5	13.7	2.5	11.2	3.5	0.3
H_2Na_2SiW	2.8	0.12	0.11	0.31	1.30	80.3	67.4	12.9	15.7	2.8	12.9	3.0	1.0
H_1Na_3SiW	2.4	0.02	0.10	0.25	2.20	83.4	74.5	8.9	13.0	1.6	11.4	2.1	1.5
H_0Na_4SiW	3.5	0.01	0.12	0.37	1.23	91.6	86.2	5.4	6.4	0.6	5.8	1.5	0.5
H_3Na_0PW	20.2	0.15	0.16	2.06	4.26	84.2	61.6	22.6	14.9	1.0	13.9	0.6	0.3
H_2Na_1PW	9.9	0.09	0.16	1.08	1.81	88.0	77.0	11.0	10.8	1.4	9.4	1.1	0.1
H_1Na_2PW	5.1	0.03	0.09	0.56	1.74	90.1	80.0	10.1	8.4	1.2	7.2	1.0	0.5
H_0Na_3PW	7.7	0.01	0.07	0.91	0.87	94.5	87.6	6.9	4.8	0.6	4.2	0.5	0.2

[a] Rates for butanal reactions on polyoxometalate clusters were measured in 1.1 kPa butanal at 573 K during steady-state reaction (time-on-stream = 305 min), subscript cluster = $H_xNa_{4-x}SiW$ or $H_yNa_{3-y}PW$, space velocity = 0.02 $mol_{butanal}$ ($mol_{cluster}$ s)$^{-1}$; [b] r_{Inter}, r_{Dehy}, and, r_{Intra} refer to the rates for primary intermolecular C=C bond formation (step a1), isomerization-dehydration (step b1), and intramolecular C=C bond formation (step c1), respectively, in Scheme 3; [c] Rate constants for butanal reactions on polyoxometalate clusters were measured in 1.1–4.4 kPa butanal at 573 K during steady-state reaction (time-on-stream = 155–605 min), subscript cluster = $H_xNa_{4-x}SiW$ or $H_yNa_{3-y}PW$, space velocity = 0.02–0.08 $mol_{butanal}$ ($mol_{cluster}$ s)$^{-1}$; [d] k_{Inter,C_4} and k_{Inter,C_8} refer to the first-order rate constants for the primary (step a1) and the secondary (step a2) intermolecular C=C bond formation, respectively, in Scheme 3; [e] Selectivities for butanal reactions were measured during steady-state reaction (time-on-stream = 305 min), defined as the amount of carbon in a product divided by the total carbon in all products; [f] Other species includes $C_7H_{14}O$, C_7H_{14}, and some unidentified species (e.g., C_{8+} species).

structures: the rate ratios of intramolecular to intermolecular C=C bond formation, r_{Intra}/r_{Inter}, are 1.5 and 2.4 on H-MFI and H-FAU, whereas those of dehydration to intermolecular C=C bond formation, r_{Dehy}/r_{Inter}, are 0.68 and 0.07 on H-MFI and H-FAU, respectively, at 573 K.[20] These distinct rate ratios between the unconfined and confined sites indicate that structural confinements promote the intramolecular C=C bond formation and isomerization–dehydration pathways, possibly via solvation of their respective transition state through van der Waals interactions in confined voids.[36]

Butanal reactions on all polyoxometalate clusters approached steady state for reaction times above 155 min, at which the rates and selectivities remained unchanged with the time-on-stream, as shown and reported elsewhere.[21] At steady-state, the predominant reaction pathway is the intermolecular C=C bond formation: the selectivities towards larger alkenals and aromatics are 97 mol% at 573 K, whereas those towards butene and butadiene are less than 4 mol% selectivities at 573 K for all $H_xNa_{4-x}SiW$ and $H_yNa_{3-y}PW$ clusters, as summarized in Table 3. Next, we correlate these rate and selectivity data to the findings from butanal and pyridine titration and IR spectroscopic studies in order to construct a mechanistic picture for these reactions.

As butanals were exposed to $H_xNa_{4-x}SiW$ (x = 0–4) and $H_yNa_{3-y}PW$ (y = 0–4) clusters, a portion of the H^+ sites were occupied by surface acetates and aromatic species, as confirmed from the evolvement of [ν_{as}(OCO)] bands at 1580 or 1577 cm^{-1} and C=C bond stretching of the aromatic rings [ν(C=C)$_{aromatic}$] at 1510 cm^{-1} during butanal adsorption and reactions at 348 K (Figure 7). The acetates remained stable at low temperatures (348 K) but desorbed from the H^+ sites to evolve into heavy aromatics during sequential heating to above 423 K, indicated by the decrease in [ν_{as}(OCO)] bands at 1580 cm^{-1} and concomitant increase in [ν(C=C)$_{aromatic}$] bands at 1600 cm^{-1} (Figure S5 a). The light aromatics (e.g., at 1510 cm^{-1}) occupying the H^+ sites could undergo sequential dehydrogenation (not shown in Scheme 3) to produce heavier aromatics (e.g., that leads to bands at 1600 cm^{-1}, Figure S5 a). The formation of heavier aromatics during the initial contact of polyoxometalate clusters to the feed leads to the decrease in the available H^+ sites after reaction at 573 K, as measured by the temperature desorption of pyridine. The site density becomes stable at 1.54 ± 0.32 mol_{H^+} ($mol_{cluster}$)$^{-1}$ for reaction times above 30 min, as reported elsewhere.[21] IR spectra of pyridine adsorption on spent $H_xNa_{4-x}SiW$ catalysts indicate that only Brønsted acid sites [with ν(Py–H^+) band at 1540 cm^{-1}] and almost no Lewis acid sites [with ν(Py–L) band at 1450 cm^{-1}] remain accessible to pyridine titrants after butanal reactions at 573 K for 30 min (Figure S7).

The rate of intermolecular C=C bond formation (step a1, Scheme 3) increases proportionally with alkanal pressures, as shown previously for butanal, pentanal, and hexanal reactions on $H_4SiW_{12}O_{40}$ polyoxometalate clusters[21] and H-FAU[20] zeolites. The intermolecular C=C bond formation step (step a1, Scheme 3) couples kinetically with intramolecular C=C bond formation (step c1, Scheme 1) and isomerization–dehydration (step b1, Scheme 3) steps. The intramolecular C=C bond formation occurs together with the intermolecular C=C bond formation, because it requires the aromatics, the secondary products, formed from the later reactions acting as the hydrogen sources in a hydride transfer step.[20,21] The isomerization–dehydration step couples with the intermolecular C=C bond formation step, because they share the co-adsorbed alkanal-alkenol pairs as the common surface intermediate.[21] For these reasons, the rates of these reactions also increase with butanal pressure.[21]

The rates (per H^+ site) for the first intermolecular C=C bond formation [$r_{Inter,C_4,per\,H^+}$, Eq. (1)], which also equal the site-time-yields of 2-ethyl-2-hexenal ($C_8H_{14}O$), are:

$$r_{Inter,C_4,per\,H^+} = k_{Inter,C_4,per\,H^+} + P_{C_4H_8O} \quad (1)$$

where $k_{\mathrm{Inter,C_4,per\,H^+}}$ is the first-order rate constant for intermolecular C=C bond formation of butanal on each H^+ site with a unit of mol $(\mathrm{mol_{H^+}\,s\,kPa})^{-1}$. This constant is related to the rate for 2-ethyl-2-hexenal ($C_8H_{14}O$) formation for each $H_xNa_{4-x}SiW$ cluster [$r_{\mathrm{Inter,C_4}}$, Eq. (2)] through Equation (3):

$$r_{\mathrm{Inter,C_4}} = k_{\mathrm{Inter,C_4}}\,P_{\mathrm{C_4H_8O}} = \lambda_{\mathrm{des,remain}}\,k_{\mathrm{Inter,C_4,per\,H^+}} + P_{\mathrm{C_4H_8O}} \quad (2)$$

$$k_{\mathrm{Inter,C_4}} = \lambda_{\mathrm{des,remain}}\,k_{\mathrm{Inter,C_4,per\,H^+}} \quad (3)$$

Here, $k_{\mathrm{Inter,C_4}}$ is the rate constant for intermolecular C=C bond formation of butanal (per $H_xNa_{4-x}SiW$ cluster, mol $(\mathrm{mol_{cluster}\,s\,kPa})^{-1}$) and $\lambda_{\mathrm{des,remain}}$ is the number of H^+ site remained after exposure to reaction mixtures [Eq. (13)], which was determined by pyridine titration followed by TPD of the adsorbed pyridine after the reactions. As shown in Figure 8, these rate constant values ($k_{\mathrm{Inter,C_4}}$, per $H_xNa_{4-x}SiW$ cluster) are directly proportional to the H^+ site densities remained after steady-state reactions ($\lambda_{\mathrm{des,remain}}$), irrespective of the initial H^+ site densities.

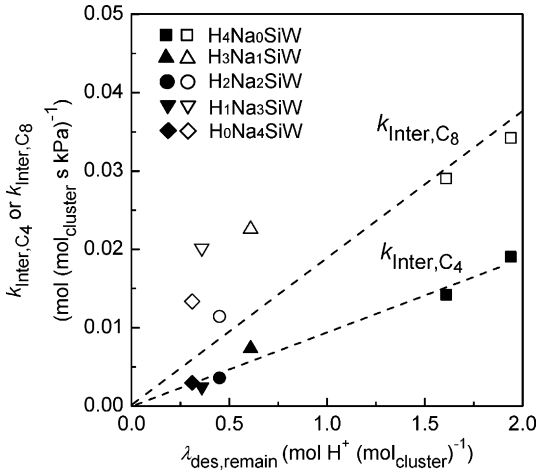

Figure 8. First-order rate constants at 573 K for the primary intermolecular C=C bond formation leading to $C_8H_{14}O$ [$k_{\mathrm{Inter,C_4}}$, Eq. (3)] and the secondary intermolecular C=C bond formation leading to $C_{12}H_{20}O$ [$k_{\mathrm{Inter,C_8}}$, Eq. (6)] on $H_xNa_{4-x}SiW$ ($x=0$–4) clusters, plotted as a function of the remaining H^+ site densities after butanal reactions [$\lambda_{\mathrm{des,remain}}$, Eq. (13), 1.1–4.4 kPa butanal, space velocity 0.02–0.08 $\mathrm{mol_{butanal}\,(mol_{cluster}\,s)^{-1}}$].

The rates (per H^+ site) for the 2,4-diethyl-2,4-octadienal (C_{12}) formation from the second intermolecular C=C bond formation ($r_{\mathrm{Inter,C_8}}$), a reaction between 2-ethyl-2-hexenal (C_8) and butanal (C_4), are related to the first-order rate constant ($k_{\mathrm{Inter,C_8}}$) and the partial pressure of 2-ethyl-2-hexenal (C_8) through [Eq. (4), (5) and (6)]:

$$r_{\mathrm{Inter,C_8,per\,H^+}} = k_{\mathrm{Inter,C_8,per\,H^+}}\,P_{\mathrm{C_8H_{14}O}} \quad (4)$$

$$r_{\mathrm{Inter,C_8}} = k_{\mathrm{Inter,C_8}}\,P_{\mathrm{C_8H_{14}O}} = \lambda_{\mathrm{des,remain}}\,k_{\mathrm{Inter,C_8,per\,H^+}}\,P_{\mathrm{C_8H_{14}O}} \quad (5)$$

$$k_{\mathrm{Inter,C_8}} = \lambda_{\mathrm{des,remain}}\,k_{\mathrm{Inter,C_8,per\,H^+}} \quad (6)$$

The values of $k_{\mathrm{Inter,C_8}}$ (per $H_xNa_{4-x}SiW$ cluster) also increase with the $\lambda_{\mathrm{des,remain}}$, as shown in Figure 8. The rate constants for the second intermolecular C=C bond formation are higher than that for the first ones ($k_{\mathrm{Inter,C_8}} > k_{\mathrm{Inter,C_4}}$), because these rate constants k_{Inter} contain the equilibrium constant term for keto–enol tautomerization (K_{taut}) and the rate constant for alkanal-alkenol pair formation (k_{AAP}), as shown elsewhere [Eq. (7)]:[21]

$$k_{\mathrm{Inter}} = K_{\mathrm{taut}}\,k_{\mathrm{AAP}} \quad (7)$$

The larger the aldehyde molecules, the higher the equilibrium constants for keto–enol tautomerization (e.g., K_{taut} equals to 1.28×10^{-4} for isobutyraldehyde versus 5.89×10^{-7} for acetaldehyde at 298 K); in addition, larger aldehydes interact more strongly with the polyoxometalate clusters through stronger van der Waals interactions. Both of these factors favor the enol formation and the co-adsorption of the enol tautomer onto the lattice oxygen site adjacent to the protonated alkenal.[37] The scatter in the rate constant dependence for the secondary condensation reactions, $k_{\mathrm{Inter,C_8}}$, in Figure 8 is caused by the much lower concentrations ($\approx$1–2 orders of magnitude lower) for 2-ethyl-2-hexenal (C_8) than butanal and therefore larger experimental errors. The linear, direct relations between these rate constants ($k_{\mathrm{Inter,C_4}}$ and $k_{\mathrm{Inter,C_8}}$) and the remaining H^+ site densities [$\lambda_{\mathrm{des,remain}}$, Eq. (13)] in Figure 8 confirm the direct involvement of H^+ sites in the intermolecular C=C bond formation step. These results also show that Na^+ ions introduced onto the polyoxometalate clusters, which replace the Brønsted acid sites, remain kinetically silent for intermolecular C=C bond formation.

The concomitant minor, secondary cyclization–dehydration reactions (e.g., steps b2 and b3, Scheme 3) form hydrocarbon species containing either 8, 12, or 16 carbon atoms (e.g., C_8H_{12} cycloalkadienes, C_{12} aromatics, and C_{16} aromatics). The carbon numbers in these products are identical to those formed from butanal stepwise condensation steps (steps a1–a3, Scheme 3). The cyclization–dehydration occurs at much lower selectivities than the intermolecular C=C bond formation on polyoxometalate clusters [e.g., carbon selectivities to alkenals and aromatics are 80.3–94.5% and 4.8–15.7%, respectively, on $H_xNa_{4-x}SiW$ and $H_yNa_{3-y}PW$, 573 K, space velocity = 0.02 $\mathrm{mol_{butanal}\,(mol_{cluster}\,s)^{-1}}$, as shown in Table 3]. Notably, carbon selectivities to larger aromatic products are much lower on H_0Na_4SiW (6.4%) and H_0Na_3PW (4.8%) than on other $H_xNa_{4-x}SiW$ ($x=1$–4) (13–15.7%) and $H_yNa_{3-y}PW$ ($y=1$–3) (8.4–14.9%) clusters, likely because H_0Na_4SiW and H_0Na_3PW clusters contain only weak H^+ sites (as shown in Figure 2). These selectivity trends indicate that stronger H^+ sites are more reactive than the weaker H^+ sites towards cyclization reactions. The lack of cyclization-dehydration reactions are in stark contrast to those on microporous crystalline solids [e.g., carbon selectivities to alkenals and aromatics are 14–16% and 20–29%, respectively, on H-FAU zeolites,[20] 573 K, space velocity = 0.03 $\mathrm{mol_{butanal}\,(mol_{H^+}\,s)^{-1}}$], which promote alkylation–dealkylation and lead in turn to aromatic and hydrocarbon species with varying carbon numbers, influenced strongly by their pore and cage sizes.[2,20]

Conclusions

Chemical titrations, IR spectroscopy, and rate measurements were used to probe the identities of reactive species and their involvements in butanal deoxygenation reactions on a series of polyoxometalate clusters [$H_xNa_{4-x}SiW_{12}O_{40}$ ($x=0$–4) and $H_yNa_{3-y}PW_{12}O_{40}$ ($y=0$–3)] with varying H^+ site densities. Butanals adsorb on these H^+ and Na^+ sites of the polyoxometalate clusters and form H^+/Na^+-bonded complexes (RC=O···H^+/Na^+). A portion of butanals at the H^+ sites reacts with vicinal framework oxygen atom and forms surface acetate, which remains as spectator species. The other portion of adsorbed butanal undergoes intermolecular C=C bond formation via aldol condensation to produce 2-ethyl-2-hexenal, which then converts into larger, unsaturated aldehydes and aromatics. Both unsaturated aldehydes and aromatics are the major products during butanal deoxygenation on polyoxometalate clusters with carbon selectivities >80 mol% towards the unsaturated aldehydes and 6–16 mol.% towards the aromatics. A linear relation between the rate constants for intermolecular C=C bond formation step (per polyoxometalate cluster) and the densities of H^+ sites remained after steady-state butanal reactions indicates that the rates are directly related to the H^+ site densities in this Brønsted acid catalyzed reaction.

Experimental Section

Preparation of supported $H_xNa_{4-x}SiW$ and $H_yNa_{3-y}PW$ clusters on SiO_2 supports

H_4Na_0SiW or H_3Na_0PW polyoxometalate (POM) clusters were supported on SiO_2 supports at a nominal loading of 0.075 $mmol_{POM}$ $(g_{SiO_2})^{-1}$ with incipient wetness impregnation method. SiO_2 support (GRACE chromatographic grade, 330 m^2g^{-1}, particle size <75 μm, pore volume 1.2 cm^3g^{-1}) was treated in ambient air at 0.17 Ks^{-1} to 773 K and held at 773 K for 5 h prior to impregnation at room temperature with a precursor solution, prepared from dissolving either $H_4SiW_{12}O_{40}$ or $H_3PW_{12}O_{40}$ (Sigma Aldrich, 99.99%, CAS #12027-43-9 or CAS #12501-23-4, respectively) in deionized water. $H_xNa_{4-x}SiW$ ($x=0$–4) and $H_yNa_{3-y}PW$ ($y=0$–3) polyoxometalate clusters were supported on SiO_2 [0.075 $mmol_{POM}$ $(g_{SiO_2})^{-1}$] using the same method, but the precursor solution used for impregnation was prepared from dissolving $H_4SiW_{12}O_{40}$ or $H_3PW_{12}O_{40}$ into an aqueous NaOH solution (0.3 $molL^{-1}$, CALEDON, CAS #1310-73-2) with its H^+-to-Na^+ molar ratio adjusted to attain the targeted value [i.e., H:Na ratio of x:(4−x) for $H_xNa_{4-x}SiW$ and y:(3−y) for $H_yNa_{3-y}PW$]. The impregnated samples were then held in closed vials for 24 h, heated to 323 K at 0.0167 Ks^{-1}, and then held isothermally at 323 K for 24 h in flowing dry air (0.1 $cm^3g^{-1}s^{-1}$, zero grade, Linde). All the samples were denoted as $H_xNa_{4-x}SiW$ ($x=0$–4) and $H_yNa_{3-y}PW$ ($y=0$–3) and the nominal H^+ site density (χ_i, subscript i=Si or P for $H_xNa_{4-x}SiW$ or $H_yNa_{3-y}PW$, respectively) reported in this manuscript was defined as [Eq. (8)]:

$$\chi_i = \frac{\text{nominal mol of } H^+}{\text{mol of cluster}} \quad (8)$$

Chemical titration with pyridine and butanal and TPD of pyridine

Chemical titration with pyridine and its sequential TPD were performed on the $H_xNa_{4-x}SiW$ ($x=0$–4) and $H_yNa_{3-y}PW$ ($y=0$–3) samples. For the pyridine titration experiment, a sample (100 mg) was supported on a quartz frit in a cylindrical microcatalytic quartz reactor (8 mm inner diameter). The sample was treated in situ under flowing He (0.83 cm^3s^{-1}) at a constant heating rate (0.083 Ks^{-1}) to 473 K and maintained isothermally at 473 K. Liquid pyridine (Sigma Aldrich, >99.9%, CAS #110-86-1) was introduced at 3.42×10^{-8} $mols^{-1}$ with a gas tight syringe (Model 006230, 0.25 cm^3, SGE) mounted on a syringe infusion pump (Model: LEGATO 100, KD Scientific) into a vaporization zone that was maintained at 391 K and located upstream from the reactor. In the vaporization zone, pyridine was evaporated and mixed with a flowing He stream (0.83 cm^3s^{-1}). The pyridine–He mixture was then introduced to the sample and the amount of pyridine in the effluent stream was quantified with a flame ionization detector (FID) without chromatographic separation. Pyridine titration was completed when the molar flow rate of pyridine in the effluent stream became identical to that of the feed stream (3.42×10^{-8} $mols^{-1}$), at which point the difference in pyridine molar flow rate between the feed and the effluent stream was less than 5%. After the pyridine titration, the sample was purged in flowing He (0.83 cm^3s^{-1}) at 473 K for 30 min and then the temperature-programmed desorption of pyridine (pyridine-TPD) was conducted. During the temperature-programmed desorption experiments, the temperature was increased to 923 K at 0.033 Ks^{-1} in flowing He (0.17 cm^3s^{-1}). During the entire period of the pyridine-TPD experiment, the amount of pyridine in the effluent stream was quantified with a flame ionization detector (FID) without chromatographic separation.

Pyridine uptakes during the pyridine chemical titration (λ_{ads}) are defined by the cumulative amount of pyridine adsorbed onto the catalysts divided by the number of polyoxometalate clusters in the sample, according to [Eq. (9)]:

$$\lambda_{ads} = \frac{\text{cumulative number of mol of pyridine adsorbed}}{\text{mol of polyoxometalate clusters}} \quad (9)$$

The pyridine-TPD profiles of H_4Na_0SiW and H_3Na_0PW show three peaks centered at approximately 550 K, 650 K, and 730 K, respectively. The amounts of pyridine desorbed from these temperature ranges reflect the adsorption strengths of pyridinium ions at the H^+ sites. Peak deconvolution of the TPD profiles by assuming Gaussian distributions leads to the site densities $\lambda_{des,1}$, $\lambda_{des,2}$, and $\lambda_{des,3}$, categorized according to the desorption temperature ranges of 500–650 K, 550–750 K, and 673–790 K, respectively. These values are determined based on the cumulative amount of pyridine desorbed in each range, obtained from fitting of the overall pyridine desorption profile to peaks with Gaussian distributions. These values are then divided by the number of polyoxometalate clusters in the sample [Eq. (10)]:

$$\lambda_{des,i} = \frac{\text{cumulative mol of pyridine desorbed in temperature range } i}{\text{mol of polyoxometalate clusters}} \quad (10)$$

where i equals 1, 2, or 3, which corresponds to the temperature ranges of 500–650 K, 550–750 K, or 673–790 K, respectively. The total amount of pyridine desorbed from fresh samples ($\lambda_{des,overall}$, 500–790 K) and the amount of pyridine desorbed from the high temperature ranges ($\lambda_{des,2-3}$, 550–790 K) are expressed by [Eq. (11)

and (12)]:

$$\lambda_{\text{des, overall}} = \lambda_{\text{des, 1}} + \lambda_{\text{des, 2}} + \lambda_{\text{des, 3}} \quad (11)$$

$$\lambda_{\text{des, 2–3}} = \lambda_{\text{des, 2}} + \lambda_{\text{des, 3}} \quad (12)$$

The spent samples after deoxygenation reaction at 573 K were subjected to pyridine titration followed by sequential TPD. The amount of pyridine desorbed from the spent sample during the TPD reflects the remaining H^+ site densities, $\lambda_{\text{des,remain}}$ [Eq. (13)]:

$$\lambda_{\text{des,remain}} = \frac{\text{cumulative mol of pyridine desorbed}}{\text{mol of polyoxometalate clusters}} \quad (13)$$

The experimental protocol for butanal titration is similar to that of pyridine, except that butanal (Sigma Aldrich, $\geq$99%, CAS #123-72-8) instead of pyridine was introduced into the vaporization zone. The vaporization zone and reactor were both maintained at 348 K. The experiment was completed when the difference in butanal molar flow rates between the reactor effluent and the feed stream was less than 5%. The amount of butanal adsorbed on the samples, α_{but}, was determined by dividing the total amount of butanal adsorbed by the number of polyoxometalate clusters contained within the sample [Eq. (14)]:

$$\alpha_{\text{but}} = \frac{\text{cumulative number of mol of adsorbed butanal}}{\text{mol of polyoxometalate clusters}} \quad (14)$$

The total amount of adsorbed butanal was calculated by subtracting the cumulative amount of butanal in the effluent stream from that of the inlet feed stream, quantified using FID.

IR spectroscopic studies of pyridine and butanal adsorption

IR spectroscopic studies were performed with a customized, stainless steel in situ transmission IR cell equipped with CaF_2 windows and capable for operating between 298 K and 773 K. The cell was mounted in a Bruker Vertex 70 spectrometer equipped with a mercury cadmium telluride (MCT) detector. The cell was connected to a vacuum line and a rotary vane pump (model 101150/11-11, Leroy Somer), which allows evacuation to less than 0.01 mbar. Powder samples were pressed into a self-supporting wafer of $\approx$10 mm in diameter and less than 0.5 mm thick, mounted into a sample holder inside the cell. Spectra were acquired in the absorbance mode at a resolution of 2 cm^{-1} and 64 scans per spectrum.

Prior to the adsorption of either pyridine or butanal, the cell was purged with flowing helium (1.67 $cm^3 s^{-1}$) for 10 min, and then heated at 0.167 $K s^{-1}$ to 573 K for another 30 min under vacuum (0.005–0.05 mbar). Afterwards, a background spectrum was obtained at 348 K under vacuum. Pyridine adsorption was performed at 473 K, by introducing sequential pyridine pulses (ca. 0.22 μmol each time, $\approx$4 to 6 pulses) until saturation. The sample chamber was evacuated under dynamic vacuum, which removed the gas phase and physisorbed pyridine, and cooled to 348 K for IR spectroscopic measurements. Similar procedures were performed for butanal adsorption at 348 K. Butanal pulses (ca. 0.32 μmol each time, $\approx$5 to 8 pulses) were introduced sequentially into the sample compartment until the catalyst surfaces became saturated, attained when the spectra did not change with additional pulses. The chamber was then evacuated under dynamic vacuum (0.01–0.1 mbar), heated step-wise to a temperature between 348 K and 573 K (348, 373, 423, 473, 523, and 573 K) and then cooled to 348 K for IR spectroscopic measurements. Quantitative comparison of the peak intensities between the catalyst samples was performed by spectrum normalization using the vibrational bands corresponded to the lattice overtone of silica at 1990 cm^{-1} and 1875 cm^{-1} following the method demonstrated previously.[22b]

Assessment of rates and selectivities for butanal deoxygenation on supported $H_xNa_{4-x}SiW$ and $H_yNa_{3-y}PW$ clusters

Butanal deoxygenation was performed in a steady-state fixed-bed microcatalytic quartz reactor (8 mm inner diameter) with plug–flow fluid hydrodynamics at 573 K. The reactor was contained within a resistively heated furnace with its temperature controlled by a digital feedback temperature controller. Catalyst samples (25 mg) were supported on a quartz frit and the bed temperature was recorded using a K-type thermocouple placed in the center (in both the axial and radial directions) of catalyst bed. Catalysts were treated in situ under flowing He (Grade 5.0, Linde, 16.7 $cm^3 g_{cat.}^{-1} s^{-1}$) by heating at 0.167 $K s^{-1}$ to 573 K. Liquid butanal was introduced into a vaporization zone using a gas tight syringe (Hamilton Gastight 1105, 5 mL) mounted on a syringe infusion pump. In the vaporization zone, butanal was evaporated and mixed with a He (Grade 5.0, Linde, 16.7 $cm^3 g_{cat.}^{-1} s^{-1}$) purge stream. The partial pressure of butanal feed was maintained at a constant value between 1.1 kPa to 4.4 kPa by controlling the infusion rate of liquid butanal. The mixture was fed to the reactor through heated transfer lines held at 473 K. Reactants and products were quantified using an on-line gas chromatograph (Agilent 7890A) with mass spectrometer (Agilent 5975C) equipped with two capillary columns of (1) Agilent HP-5MS (190091S-433, 30 m, 0.25 mm ID, 0.25 μm film), connected to a thermal conductivity detector (TCD) and flame ionization detector (FID) in series, and (2) HP-5 (19091J-413, 30 m, 0.32 mm ID, 0.25 μm film) connected to a mass selective detector (MSD).

Acknowledgements

The work was supported by the Natural Sciences and Engineering Research Council of Canada (NSERC), Canada Foundation for Innovation (CFI), Valmet, Abellon CleanEnergy; F.L. acknowledges Hatch Graduate Scholarship for Sustainable Energy Research and Ontario Graduate Scholarship for supports.

Keywords: acidity · aldol reaction · IR spectroscopy · polyoxometalates · tautomerism

[1] a) D. Mohan, C. U. Pittman, P. H. Steele, *Energy Fuels* **2006**, *20*, 848–889; b) T. Q. Hoang, X. Zhu, T. Sooknoi, D. E. Resasco, R. G. Mallinson, *J. Catal.* **2010**, *271*, 201–208; c) S. A. W. Hollak, K. P. de Jong, D. S. van Es, *ChemCatChem* **2014**, *6*, 2648–2655; d) G. Li, F. Zhang, L. Chen, C. Zhang, H. Huang, X. Li, *ChemCatChem* **2015**, *7*, 2646–2653; e) J. Dai, X. Fu, L. Zhu, J. Tang, X. Guo, C. Hu, *ChemCatChem* **2016**, *8*, 1379–1385.

[2] F. Lin, Y.-H. Chin, *J. Catal.* **2014**, *311*, 244–256.

[3] A. G. Gayubo, A. T. Aguayo, A. Atutxa, R. Aguado, M. Olazar, J. Bilbao, *Ind. Eng. Chem. Res.* **2004**, *43*, 2619–2626.

[4] C. B. Warren, A. B. Marin, J. F. Butler, Vol. US5665781 A, International Flavors & Fragrances Inc., The University Of Florida, **1997**.

[5] a) W. Pinkenhagen, Vol. US4381410 A, Firmenich Sa, **1983**; b) W. Pickenhagen, A. Velluz, Vol. US4324809 A, Firmenich Sa, **1982**.

[6] R. Veltri, G. B. Fodor, Vol. US5098933 A, Theracel Corporation, **1992**.

[7] a) E. Dumitriu, N. Bilba, M. Lupascu, A. Azzouz, V. Hulea, G. Cirje, D. Nibou, *J. Catal.* **1994**, *147*, 133–139; b) E. Dumitriu, V. Hulea, N. Bilba, G. Carja, A. Azzouz, *J. Mol. Catal.* **1993**, *79*, 175–185.

[8] a) H. Tsuji, F. Yagi, H. Hattori, H. Kita, *J. Catal.* **1994**, *148*, 759 – 770; b) H. E. Swift, J. E. Bozik, F. E. Massoth, *J. Catal.* **1969**, *15*, 407 – 416.
[9] C. D. Chavez Diaz, S. Locatelli, E. E. Gonzo, *Zeolites* **1992**, *12*, 851 – 857.
[10] a) R. J. Gorte, D. White, A. I. Biaglow, W. E. Farneth, J. Šepa, *J. Catal.* **1997**, *167*, 300 – 302; b) L. Kubelková, J. Cejka, J. Novakova, *Zeolites* **1991**, *11*, 48 – 53; c) S. Beran, L. Kubelkova, *J. Mol. Catal.* **1987**, *39*, 13 – 19; d) D. Farcaşiu, *J. Catal.* **1996**, *160*, 309 – 313.
[11] D. H. Barich, J. B. Nicholas, T. Xu, J. F. Haw, *J. Am. Chem. Soc.* **1998**, *120*, 12342 – 12350.
[12] C. M. Nguyen, M.-F. Reyniers, G. B. Marin, *J. Phys. Chem. C* **2011**, *115*, 8658 – 8669.
[13] C. Liu, T. J. Evans, L. Cheng, M. R. Nimlos, C. Mukarakate, D. J. Robichaud, R. S. Assary, L. A. Curtiss, *J. Phys. Chem. C* **2015**, *119*, 24025 – 24035.
[14] J. R. Sohn, J. S. Han, J. S. Lim, *Appl. Surf. Sci.* **2005**, *252*, 858 – 865.
[15] X. Solans-Monfort, J. Bertran, V. Branchadell, M. Sodupe, *J. Phys. Chem. B* **2002**, *106*, 10220 – 10226.
[16] M. Xu, W. Wang, M. Hunger, *Chem. Commun.* **2003**, 722 – 723.
[17] L. Cheng, X. P. Ye, *Catal. Lett.* **2009**, *130*, 100 – 107.
[18] H. Atia, U. Armbruster, A. Martin, *J. Catal.* **2008**, *258*, 71 – 82.
[19] a) J. Macht, M. J. Janik, M. Neurock, E. Iglesia, *Angew. Chem. Int. Ed.* **2007**, *46*, 7864 – 7868; *Angew. Chem.* **2007**, *119*, 8010 – 8014; b) J. Macht, M. J. Janik, M. Neurock, E. Iglesia, *J. Am. Chem. Soc.* **2008**, *130*, 10369 – 10379.
[20] F. Lin, Y.-H. Chin, *J. Catal.* **2016**, *341*, 136 – 148.
[21] F. Lin, Y.-H. Chin, *ACS Catal.* **2016**, *6*, 6634 – 6650.
[22] a) G. Busca, *Phys. Chem. Chem. Phys.* **1999**, *1*, 723 – 736; b) S. Zheng, H. R. Heydenrych, A. Jentys, J. A. Lercher, *J. Phys. Chem. B* **2002**, *106*, 9552 – 9558; c) E. P. Parry, *J. Catal.* **1963**, *2*, 371 – 379.
[23] B. K. Hodnett, J. B. Moffat, *J. Catal.* **1984**, *88*, 253 – 263.
[24] J. J. Borrás-Almenar, E. Coronado, A. Müller, M. Pope, *Polyoxometalate Molecular Science*, Kluwer, Boston, **2003**.
[25] M. Brändle, J. Sauer, *J. Am. Chem. Soc.* **1998**, *120*, 1556 – 1570.
[26] NIST Chemistry WebBook: NIST Standard Reference Database Number 69, http://webbook.nist.gov/chemistry/. (accessed on Oct 11, **2016**).
[27] G. O. Pates, L. Guler, J. J. Nash, H. I. Kenttämaa, *J. Am. Chem. Soc.* **2011**, *133*, 9331 – 9342.
[28] a) M. S. Zanuttini, B. O. D. Costa, C. A. Querini, M. A. Peralta, *Appl. Catal. A* **2014**, *482*, 352 – 361; b) G. Rumplmayr, J. A. Lercher, *Zeolites* **1990**, *10*, 283 – 287.
[29] Z. Wu, A. K. P. Mann, M. Li, S. H. Overbury, *J. Phys. Chem. C* **2015**, *119*, 7340 – 7350.
[30] J. Raskó, J. Kiss, *Appl. Catal. A* **2005**, *287*, 252 – 260.
[31] J. E. Rekoske, M. A. Barteau, *Langmuir* **1999**, *15*, 2061 – 2070.
[32] J. Szanyi, J. H. Kwak, R. A. Moline, C. H. F. Peden, *J. Phys. Chem. B* **2004**, *108*, 17050 – 17058.
[33] A. Yee, S. J. Morrison, H. Idriss, *J. Catal.* **1999**, *186*, 279 – 295.
[34] A. Bielanski, J. Datka, B. Gil, A. Malecka-Lubanska, A. Micek-Ilnicka, *Phys. Chem. Chem. Phys.* **1999**, *1*, 2355 – 2360.
[35] A. Bielański, J. Datka, B. Gil, A. Małecka-Lubańska, A. Micek-Ilnicka, *Catal. Lett.* **1999**, *57*, 61 – 64.
[36] a) A. J. Jones, S. I. Zones, E. Iglesia, *J. Phys. Chem. C* **2014**, *118*, 17787 – 17800; b) R. Gounder, E. Iglesia, *Chem. Commun.* **2013**, *49*, 3491 – 3509.
[37] a) Y. Apeloig, D. Arad, Z. Rappoport, *J. Am. Chem. Soc.* **1990**, *112*, 9131 – 9140; b) Y. Chiang, A. J. Kresge, P. A. Walsh, *J. Am. Chem. Soc.* **1982**, *104*, 6122 – 6123; c) J. R. Keeffe, A. J. Kresge, N. P. Schepp, *J. Am. Chem. Soc.* **1990**, *112*, 4862 – 4868; d) B. L. Newalkar, N. V. Choudary, P. Kumar, S. Komarneni, T. S. G. Bhat, *Chem. Mater.* **2002**, *14*, 304 – 309.

Manuscript received: August 22, 2016
Revised: November 10, 2016
Accepted Article published: November 17, 2016
Final Article published: January 2, 2017